



An Eulerian–Lagrangian approach for simulating explosions of energetic devices

J.E. Guilkey ^{*}, T.B. Harman, B. Banerjee

Department of Mechanical Engineering, University of Utah, Salt Lake City, UT 84112, United States

Received 5 December 2006; accepted 12 January 2007

Available online 26 March 2007

Abstract

An approach for the simulation of explosions of “energetic devices” is described. In this context, an energetic device is a metal container filled with a high explosive (HE). Examples include bombs, mines, rocket motors or containers used in storage and transport of HE material. Explosions may occur due to detonation or deflagration of the HE material, with initiation resulting from either mechanical or thermal input. This approach is applicable to a wide range of fluid–structure interaction scenarios, the application to energetic devices is chosen because it demonstrates the full capability of this methodology.

Simulations of this type are characterized by a number of interesting and challenging behaviors. These include the transformation of the solid HE into highly pressurized gaseous products that initially occupy regions which formerly contained only solid material. This rapid pressurization of the container leads to large deformations at high strain rates and eventual case rupture. Once the container breaks apart, the highly pressurized product gas that escapes the failing container generates shock waves that propagate through the initially quiescent surrounding fluid.

The approach, which uses a finite-volume, multi-material compressible CFD formulation, within which solid materials are represented using a particle method known as the Material Point Method, is described, including certain of the sub-grid models required to close the governing equations. Results are first presented for “rate stick” and “cylinder test” scenarios, each of which involves detonating unconfined and confined HE material, respectively. Experimental data are available for these configurations and as such they serve as validation tests. Finally, results from an unvalidated “fast cookoff” simulation in which the HE is initiated by thermal input, which causes deflagration, are shown.

© 2007 Elsevier Ltd. All rights reserved.

Keywords: Fluid–structure interaction; Material point method; Energetic device; Explosion modeling; Computational fluid dynamics; Multi-material dynamics

1. Introduction

The work presented here describes a numerical approach for “full physics” simulations of dynamic fluid–structure interactions involving large deformations and material transformations (e.g., phase change). “Full physics” refers to problems involving strong interactions between the fluid field and solid field temperatures and velocities, with a full Navier–Stokes representation of fluid

materials and the transient, nonlinear response of solid materials. These interactions may include chemical or physical transformation between the solid and fluid fields.

Approaches to fluid structure interaction (FSI) problems are typically divided into two classes. “Separated” approaches treat individual materials as occupying distinct regions of space, with interactions occurring only at material interfaces. The details of those interactions vary between implementations, and are often a function of the degree, or “strength” of the coupling between the fluid and solid fields. Because of the separated nature of the materials, only one set of state variables is needed at any point in space, since only one material is allowed to exist

^{*} Corresponding author. Tel.: +1 801 581 8709; fax: +1 801 585 9826.
E-mail address: james.guilkey@utah.edu (J.E. Guilkey).

at that point. “Averaged” model approaches allow *all* materials to exist at any point in space with some probability. Variables describing the material state vary continuously throughout the computational domain, thus, the state of every material is defined at every point in space. Distinct material interfaces are not defined, rather the interaction between materials is computed in an average sense, and, as such, interactions among materials may take place anywhere.

While both the separated and averaged model approaches have their respective merits, the averaged model, when carried out on an Eulerian grid, allows arbitrary distortion of materials and material interfaces. However, these distortions can be catastrophic for the solid material, as the deformation history of the solid must be transported through the Eulerian grid. This transport can lead to non-physical stresses and the interface between materials is also subject to diffusion. The latter problem can be mitigated via surface tracking and the use of a single valued velocity field [1,2], but this does not eliminate the problems of stress transport.

The approach described here uses the averaged model approach and addresses the issue of stress transport by integrating the state of the solid field in the “material” frame of reference through use of the Material Point Method (MPM) [3,4]. MPM is a particle method for solid mechanics that allows the solid field to undergo arbitrary distortion. Because the fluid state is integrated in the Eulerian frame, it can also undergo arbitrary distortion. MPM uses a computational “scratchpad” grid to advance the solution to the equations of motion, and by choosing to use the same grid used in the Eulerian frame of reference, interactions among the materials are facilitated on this common computational framework. By choosing to use an infinitely fast rate of momentum transfer between the materials, the single velocity field limit is obtained, and the interface between materials is limited to, at most, a few cells. Thus, in the differential limit, the separated model can be recovered. This means that with sufficient grid resolution, the accuracy of the separated model and the robustness of the averaged model can be enjoyed simultaneously.

The theoretical and algorithmic basis for the fluid structure interaction simulations presented here is based on a body of work of several investigators at Los Alamos National Laboratory, primarily Bryan Kashiwa, Rick Rauenzahn and Matt Lewis. Several reports by these researchers are publicly available and are cited herein. It is largely through our personal interactions that we have been able to bring these ideas to bear on the simulations described herein.

An exposition of the governing equations is given in the next section, followed by an algorithmic description of the solution of those equations. This description is first done separately for the materials in the Eulerian and Lagrangian frames of reference, before details associated with the integrated approach are given. Because this manuscript is focused on explosions of energetic devices, some of the

models used to close the governing equations are described briefly. Finally, results from three calculations are presented. The first two of these are intended to serve as validation of the general approach and the models used, while the third is an unvalidated demonstration calculation. The reader is encouraged to browse Section 5 at this point to better appreciate the direction that the subsequent development is headed.

2. Governing equations

The governing multi-material model equations are stated and described, but not developed, here. Their development can be found in [5]. Here, our intent is to identify the quantities of interest, of which there are 8, as well as those equations (or closure models) which govern their behavior. Consider a collection of N materials, and let the subscript r signify one of the materials, such that $r = 1, 2, 3, \dots, N$. In an arbitrary volume of space $V(\mathbf{x}, t)$, the averaged thermodynamic state of a material is given by the vector $[M_r, \mathbf{u}_r, e_r, T_r, v_r, \theta_r, \boldsymbol{\sigma}_r, p]$, the elements of which are the r -material mass, velocity, internal energy, temperature, specific volume, volume fraction, stress, and the equilibration pressure. The r -material averaged density is $\rho_r = M_r/V$. The rate of change of the state in a volume moving with the velocity of r -material is:

$$\frac{1}{V} \frac{D_r M_r}{Dt} = \sum_{s=1}^N \Gamma_{rs} \quad (1)$$

$$\frac{1}{V} \frac{D_r(M_r \mathbf{u}_r)}{Dt} = \theta_r \nabla \cdot \boldsymbol{\sigma} + \nabla \cdot \theta_r (\boldsymbol{\sigma}_r - \boldsymbol{\sigma}) + \rho_r \mathbf{g} + \sum_{s=1}^N \mathbf{f}_{rs} + \sum_{s=1}^N \mathbf{u}_{rs}^+ \Gamma_{rs} \quad (2)$$

$$\begin{aligned} \frac{1}{V} \frac{D_r(M_r e_r)}{Dt} &= -\rho_r p \frac{D_r v_r}{Dt} + \theta_r \boldsymbol{\tau}_r : \nabla \mathbf{u}_r - \nabla \cdot \mathbf{j}_r \\ &+ \sum_{s=1}^N q_{rs} + \sum_{s=1}^N h_{rs}^+ \Gamma_{rs} \end{aligned} \quad (3)$$

Eqs. (1)–(3) are the averaged model equations for mass, momentum, and internal energy of r -material, in which $\boldsymbol{\sigma}$ is the mean mixture stress, taken here to be isotropic, so that $\boldsymbol{\sigma} = -p\mathbf{I}$ in terms of the hydrodynamic pressure p . The effects of turbulence have been explicitly omitted from these equations, and the subsequent solution, for the sake of simplicity. However, including the effects of turbulence is not precluded by either the model or the solution method used here.

In Eq. (2) the term $\sum_{s=1}^N \mathbf{f}_{rs}$ signifies a model for the momentum exchange among materials. This term results from the deviation of the r -field stress from the mean stress, averaged, and is typically modeled as a function of the relative velocity between materials at a point. (For a two material problem this term might look like $\mathbf{f}_{12} = K_{12}\theta_1\theta_2(\mathbf{u}_1 - \mathbf{u}_2)$ where the coefficient K_{12} determines the rate at which momentum is transferred between materials). Likewise, in Eq. (3), $\sum_{s=1}^N q_{rs}$ represents an exchange of heat energy

among materials. For a two material problem $q_{12} = H_{12}\theta_1\theta_2(T_2 - T_1)$ where T_r is the r -material temperature and the coefficient H_{rs} is analogous to a convective heat transfer rate coefficient. The heat flux is $\mathbf{j}_r = -\rho_r b_r \nabla T_r$ where the thermal diffusion coefficient b_r includes both molecular and turbulent effects (when the turbulence is included).

In Eqs. (1)–(3) the term Γ_{rs} is the rate of mass conversion from s -material into r -material, for example, the burning of a solid reactant into gaseous products. The rate at which mass conversion occurs is governed by a reaction model, two examples of which are given in Section 4.1. In Eqs. (2) and (3), the velocity \mathbf{u}_{rs}^+ and the enthalpy h_{rs}^+ are those of the s -material that is converted into r -material. These are simply the mean values associated with the donor material.

The temperature T_r , specific volume v_r , volume fraction θ_r , and hydrodynamic pressure p are related to the r -material mass density, ρ_r , and specific internal energy, e_r , by way of equations of state. The four relations for the four quantities (T_r , v_r , θ_r , p) are:

$$e_r = e_r(v_r, T_r) \quad (4)$$

$$v_r = v_r(p, T_r) \quad (5)$$

$$\theta_r = \rho_r v_r \quad (6)$$

$$0 = 1 - \sum_{s=1}^N \rho_s v_s \quad (7)$$

Eqs. (4) and (5) are, respectively, the caloric and thermal equations of state. Eq. (6) defines the volume fraction, θ , as the volume of r -material per total material volume, and with that definition, Eq. (7), referred to as the multi-material equation of state, follows. It defines the unique value of the hydrodynamic pressure p that allows arbitrary masses of the multiple materials to identically fill the volume V . This pressure is called the “equilibration” pressure, p_{eq} [6].

A closure relation is still needed for the material stress σ_r . For a fluid $\sigma_r = -p\mathbf{I} + \tau_r$ where the deviatoric stress is well known for Newtonian fluids. For a solid, the material stress is the Cauchy stress. The Cauchy stress is computed using a solid constitutive model and may depend on the rate of deformation, the current state of deformation (\mathbf{E}), the temperature, and possibly a number of history variables. Such a relationship may be expressed as:

$$\sigma_r \equiv \sigma_r(\mathbf{V}\mathbf{u}_r, \mathbf{E}_r, T_r, \dots) \quad (8)$$

The approach described here imposes no restrictions on the types of constitutive relations that can be considered. More specific discussion of some of the models used in this work is found in Section 4.

Eqs. (1)–(8) form a set of eight equations for the eight-element state vector $[M_r, \mathbf{u}_r, e_r, T_r, v_r, \theta_r, \sigma_r, p]$, for any arbitrary volume of space V moving with the r -material velocity. The approach described here uses the reference frame most suitable for a particular material type. As such, there is no guarantee that arbitrary volumes will remain coincident for materials described in different reference frames.

This problem is addressed by treating the specific volume as a dynamic variable of the material state which is integrated forward in time from initial conditions. In so doing, at any time, the total volume associated with all of the materials is given by:

$$V_t = \sum_{r=1}^N M_r v_r \quad (9)$$

so the volume fraction is $\theta_r = M_r v_r / V_t$ (which sums to one by definition). An evolution equation for the r -material specific volume, derived from the time variation of Eqs. (4)–(7), has been developed in [5]. It is stated here as:

$$\begin{aligned} \frac{1}{V} \frac{D_r(M_r v_r)}{Dt} &= f_r^\theta \nabla \cdot \mathbf{u} + \left[v_r \Gamma_r - f_r^\theta \sum_{s=1}^N v_s \Gamma_s \right] \\ &+ \left[\theta_r \beta_r \frac{D_r T_r}{Dt} - f_r^\theta \sum_{s=1}^N \theta_s \beta_s \frac{D_s T_s}{Dt} \right] \end{aligned} \quad (10)$$

where $f_r^\theta = \frac{\theta_r \kappa_r}{\sum_{s=1}^N \theta_s \kappa_s}$, β is the constant pressure thermal expansivity, and κ_r is the r -material bulk compressibility.

The evaluation of the multi-material equation of state (Eq. (7)) is still required in order to determine an equilibrium pressure that results in a common value for the pressure, as well as specific volumes that fill the total volume identically.

3. Numerical implementation

A description of the means by which numerical solutions to the equations in Section 2 are found is presented next. This begins with separate, brief, overviews of the methodologies used for the Eulerian and Lagrangian reference frames. The algorithmic details necessary for integrating them to achieve a tightly coupled fluid–structure interaction capability is provided in Section 3.3.

3.1. Eulerian multi-material method

The Eulerian method implemented here is a cell-centered, finite-volume, multi-material version of the ICE (for Implicit, Continuous fluid, Eulerian) method [7] developed by Kashiwa and others at Los Alamos National Laboratory [8]. “Cell-centered” means that all elements of the state are colocated at the grid cell-center (in contrast to a staggered grid, in which velocity components may be centered at the faces of grid cells, for example). This colocation is particularly important in regions where a material mass is vanishing. By using the same control volume for mass and momentum it can be assured that as the material mass goes to zero, the momentum also goes to zero at the same rate, leaving a well defined velocity. The technique is fully compressible, allowing wide generality in the types of problems that can be addressed.

Our use of the cell-centered ICE method employs time splitting: first, a Lagrangian step updates the state due to

the physics of the conservation laws (i.e., right hand side of Eqs. (1)–(3)); this is followed by an Eulerian step, in which the change due to advection is evaluated. For solutions in the Eulerian frame, the method is well developed and described in [8].

In the mixed frame approach used here, a modification to the multi-material equation of state is needed. Eq. (7) is unambiguous when all materials are fluids or in cases of a flow consisting of dispersed solid grains in a carrier fluid. However in fluid–structure problems the stress state of a submerged structure may be strongly directional, and the isotropic part of the stress has nothing to do with the hydrodynamic (equilibration) pressure p_{eq} . The equilibrium that typically exists between a fluid and a solid is at the interface between the two materials: there the normal part of the traction equals the pressure exerted by the fluid on the solid over the interface. Because the orientation of the interface is not explicitly known at any point (it is effectively lost in the averaging) such an equilibrium cannot be computed.

The difficulty, and the modification that resolves it, can be understood by considering a solid material in tension coexisting with a gas. For solid materials, the equation of state is the bulk part of the constitutive response (that is, the isotropic part of the Cauchy stress vs. specific volume and temperature). If one attempts to equate the isotropic part of the stress with the fluid pressure, there exist regions in pressure–volume space for which Eq. (7) has no physical solutions (because the gas pressure is only positive). This can be seen schematically in Fig. 1, which sketches equations of state for a gas and a solid, at an arbitrary temperature.

Recall that the isothermal compressibility is the negative slope of the specific volume vs. pressure. Embedded struc-

tures considered here are solids and, at low pressure, possess a much smaller compressibility than the gasses in which they are submerged. Nevertheless the variation of condensed phase specific volume can be important at very high pressures, where the compressibilities of the gas and condensed phase materials can become comparable (as in a detonation wave, for example). Because the speed of shock waves in materials is determined by their equations of state, obtaining accurate high pressure behavior is an important goal of our FSI studies.

To compensate for the lack of directional information for the embedded surfaces, we evaluate the solid phase equations of state in two parts. Above a specified positive threshold pressure (typically 1 atmosphere), the full equation of state is respected; below that threshold pressure, the solid phase pressure follows a polynomial chosen to be C^1 continuous at the threshold value and which approaches zero as the specific volume becomes large. The effect is to decouple the solid phase specific volume from the stress when the isotropic part of the stress falls below a threshold value. In regions of coexistence at states below the threshold pressure, p tends to behave according to the fluid equation of state (due to the greater compressibility) while in regions of pure condensed phase material p tends rapidly toward zero and the full material stress dominates the dynamics as it should.

3.2. The Material Point Method

Solid materials with history dependent constitutive relations are more conveniently treated in the Lagrangian frame. Here we briefly describe a particle method known as the Material Point Method (MPM) which is used to evolve the equations of motion for the solid phase materials. MPM is a powerful technique for computational solid mechanics, and has found favor in applications involving complex geometries [9], large deformations [10] and fracture [11], to name a few. After the description of MPM, its incorporation within the multi-material solution is described in Section 3.3.

Originally described by Sulsky et al. [3,4], MPM is a particle method for structural mechanics simulations. MPM is an extension to solid mechanics of FLIP [12], which is a particle-in-cell (PIC) method for fluid flow simulation. The method typically uses a cartesian grid as a computational scratchpad for computing spatial gradients. This same grid also functions as an updated Lagrangian grid that moves with the particles during advection and thus eliminates the diffusion problems associated with advection on an Eulerian grid. At the end of a timestep, the grid is reset to the original, regularly ordered, position.

In explicit MPM, the equations of motion are cast in the form [4]:

$$\mathbf{m}\mathbf{a} = \mathbf{F}^{\text{ext}} - \mathbf{F}^{\text{int}} \quad (11)$$

where \mathbf{m} is the mass matrix, \mathbf{a} is the acceleration vector, \mathbf{F}^{ext} is the external force vector (sum of the body forces and

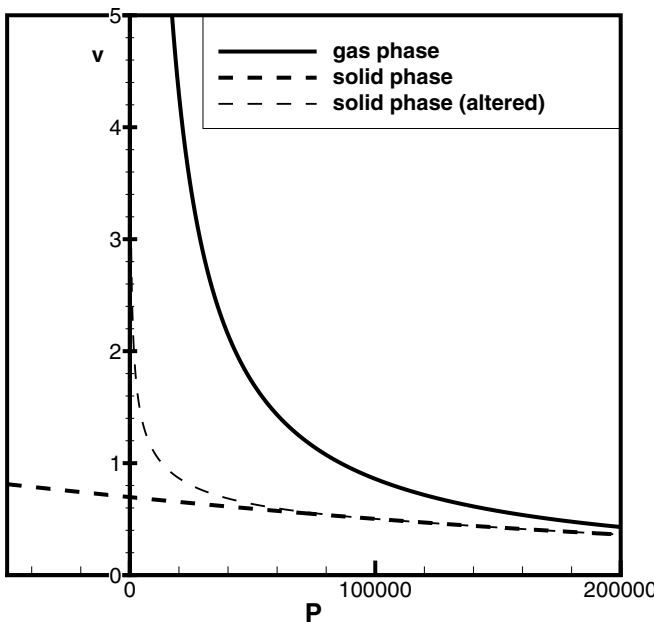


Fig. 1. Specific volume vs. pressure for a gas phase material and a solid phase material. Light dashed line reflects an altered solid phase equation of state to keep all materials in positive equilibration pressure space.

tractions), and \mathbf{F}^{int} is the internal force vector resulting from the divergence of the material stresses.

The solution procedure begins by projecting the particle state to the nodes of the computational grid, to form the mass matrix \mathbf{m} and to find the nodal external forces \mathbf{F}^{ext} , and velocities, \mathbf{v} . In practice, a lumped mass matrix is usually used. These quantities are calculated at individual nodes by the following equations, where the \sum_p represents a summation over all particles:

$$m_i = \sum_p S_{ip} m_p, \quad \mathbf{v}_i = \frac{\sum_p S_{ip} m_p \mathbf{v}_p}{m_i}, \quad \mathbf{F}_i^{\text{ext}} = \sum_p S_{ip} \mathbf{F}_p^{\text{ext}} \quad (12)$$

and i refers to individual nodes of the grid. m_p is the particle mass, \mathbf{v}_p is the particle velocity, and $\mathbf{F}_p^{\text{ext}}$ is the external force on the particle. S_{ip} is the shape function of the i th node evaluated at \mathbf{x}_p . Traditionally, standard tri-linear shape functions are used, but recently smoother interpolants, as described in [13], have yielded improved results.

A velocity gradient, $\nabla \mathbf{v}_p$ is computed at the particles using the velocities projected to the grid:

$$\nabla \mathbf{v}_p = \sum_i \mathbf{G}_{ip} \mathbf{v}_i \quad (13)$$

where \mathbf{G}_{ip} is the gradient of the shape function of the i th node evaluated at \mathbf{x}_p .

This is used as input to a constitutive model which is evaluated on a per particle basis, the result of which is the Cauchy stress at each particle, σ_p . With this, the internal force due to the divergence of the stress is calculated via:

$$\mathbf{F}_i^{\text{int}} = \sum_p \mathbf{G}_{ip} \sigma_p V_p \quad (14)$$

where V_p is the particle volume.

Eq. (11) can then be solved for \mathbf{a} . An explicit forward Euler method is used for the time integration:

$$\mathbf{v}^L = \mathbf{v} + \mathbf{a} \Delta t \quad (15)$$

and the particle position and velocity are explicitly updated by:

$$\mathbf{v}_p(t + \Delta t) = \mathbf{v}_p(t) + \sum_i S_{ip} \mathbf{a}_i \Delta t \quad (16)$$

$$\mathbf{x}_p(t + \Delta t) = \mathbf{x}_p(t) + \sum_i S_{ip} \mathbf{v}_i^L \Delta t \quad (17)$$

This completes one timestep.

By describing and implementing MPM in an independent fashion, validation of the method itself as well as sub-models (e.g., constitutive models and contact) is simplified. However, we emphasize that its use here is for selected material field description within the general multi-material formulation. This integration is described next.

3.3. Integration of MPM within the Eulerian multi-material formulation

An important feature of this work is the ability to represent a material in either the Lagrangian or Eulerian frame.

This allows treating specific phases in their traditionally preferred frame of reference. The Material Point Method, is used to time advance solid materials that are best described in a Lagrangian reference frame. By choosing the background grid used to update the solid materials to be the same grid used in the multi-material Eulerian description, all interactions among materials can be computed in the common framework, according to the momentum and heat exchange terms in Eqs. (2) and (3). This results in a robust and tightly coupled solution for interacting materials with very different responses.

To illustrate how the integration is accomplished in an algorithmic fashion the explicit steps for advancing a fluid–structure interaction problem from time t to time $t + \Delta t$ are described below.

- (1) *Project particle state to grid:* A simulation timestep begins by interpolating the particle description of the solid to the grid. This starts with a projection of particle data to grid vertices, or nodes, as described in Eq. (12), and is followed by a subsequent projection from the nodes to the cell-centers, given by (for velocity):

$$\mathbf{u}_j = \frac{\sum_{i=1}^N w_{ij} m_i \mathbf{u}_i}{\sum_{i=1}^N w_{ij} m_i} \quad (18)$$

Since our work uses a cartesian grid, $N = 8$. $w_{ij} = \frac{1}{8}$, except for those nodes at symmetry boundaries where the weight of those nodes must be doubled in order to achieve the desired effect.

- (2) *Compute the equilibration pressure:* While Eq. (7) and the surrounding discussion describes the basic process, one specific point warrants further explanation. In particular, the manner in which each material's volume fraction is computed is crucial. Because the solid and fluid materials are evolved in different frames of reference, the total volume of material in a cell is not necessarily equal to the volume of a computational cell. Material volume is tracked by evolving the specific volume for each material according to Eq. (10). The details of this are further described in step 11.

With the materials' masses and specific volumes, material volume can be computed ($V_r = M_r v_r$) and summed to find the total material volume. The volume fraction θ_r is then computed as the volume of r -material per total material volume. With this, the solution of Eq. (7) can be carried out at each cell using a Newton–Raphson technique [14], which results in new values for the equilibrium pressure, p_{eq} , volume fraction, θ_r and specific volume, v_r .

- (3) *Compute face-centered velocities, u_r^* , for the Eulerian advection:* At this point, fluxing velocities are computed at each cell face. The expression for this is based on a time advanced estimate for the cell-centered velocity. A full development can be found in

[8,5] but here, only the result is given. The following expression gives the face normal velocity component based on adjacent cell values:

$$u_r^* = \frac{\rho_{r_L} u_{r_L} + \rho_{r_R} u_{r_R}}{\rho_{r_L} + \rho_{r_R}} - \left(\frac{2v_{r_L} v_{r_R} \Delta t}{v_{r_L} + v_{r_R}} \right) \left(\frac{p_{eq_R} - p_{eq_L}}{\Delta x} \right) + g \Delta t \quad (19)$$

The first term above is a mass weighted average of the logically left and right cell-centered velocities, the second is a pressure gradient acceleration term, and the third is acceleration due to the component of gravity in the face normal direction. Not shown explicitly is the necessary momentum exchange at the face-centers. This is done on the faces in the same manner as described subsequently in step 10 for the cell-centered momentum exchange.

- (4) *Multiphase chemistry*: Compute sources of mass, momentum, energy and specific volume as a result of phase changing chemical reactions for each r -material, Γ_r , $u_r \Gamma_r$, $e_r \Gamma_r$ and $v_r \Gamma_r$. Specifics of the calculation of Γ_r are model dependent, and examples are given in Section 4.1. Care must be taken to reduce the momentum, internal energy and volume of the reactant by an amount proportional to the mass consumed each timestep, so that those quantities are depleted at the same rate as the mass. When the reactant material is described by particles, decrementing the particle mass automatically decreases the momentum and internal energy of that particle by the appropriate amount. This mass, momentum and internal energy is transferred to the product material's state, and the volume fraction for the reactant and product materials is recomputed.
- (5) *Compute an estimate of the time advanced pressure, p* : Based on the volume of material being added to (or subtracted from) a cell in a given timestep, an increment to the cell-centered pressure is computed using:

$$\Delta p = \Delta t \frac{\sum_{r=1}^N v_r \Gamma_r - \sum_{r=1}^N \nabla \cdot (\theta_r^* u_r^*)}{\sum_{r=1}^N \theta_r \kappa_r} \quad (20)$$

$$p = p_{eq} + \Delta p \quad (21)$$

where κ_r is the r -material bulk compressibility. The first term in the numerator of Eq. (20) represents the change in volume due to reaction, i.e., a given amount of mass would tend to occupy more volume in the gas phase than the solid phase, leading to an increase in pressure. The second term in the numerator represents the net change in volume of material in a cell due to flow into or out of the cell. The denominator is essentially the mean compressibility of the mixture of materials within that cell. This increment in pressure is added to the equilibrium pressure computed in step 2 and is the pressure used for the remainder of the current timestep. Again, the details leading to this equation can be found in [8].

- (6) *Face centered pressure p^** : The calculation of p^* is discussed at length in [5]. For this work, it is computed using the updated pressure by:

$$p^* = \left(\frac{p_L}{\rho_L} + \frac{p_R}{\rho_R} \right) \Big/ \left(\frac{1}{\rho_L} + \frac{1}{\rho_R} \right) \quad (22)$$

where the subscripts L and R refer to the logically left and right cell-centered values, respectively, and ρ is the sum of all materials' densities in that cell. This will be used subsequently for the computation of the pressure gradient, ∇p^* .

- (7) *Material stresses*: For the solid, we calculate the velocity gradient at each particle based on the grid velocity (Eq. (13)) for use in a constitutive model to compute particle stress. Fluid stresses are computed on cell faces based on cell-centered velocities.
- (8) *Accumulate sources of mass, momentum and energy at cell-centers*: These terms are of the form:

$$\Delta(m)_r = \Delta t V \sum_{s=1, s \neq r}^N \Gamma_s \quad (23)$$

$$\Delta(m\mathbf{u})_r = -\Delta t V \left[\theta_r \nabla p^* + \nabla \cdot \theta_r (\boldsymbol{\sigma}_r - \boldsymbol{\sigma}) + \sum_{s=1, s \neq r}^N \mathbf{u}_s \Gamma_s \right] \quad (24)$$

$$\Delta(me)_r = -\Delta t V \left[f_r^\theta p \sum_{s=1}^N \nabla \cdot (\theta_r^* \mathbf{u}_r^*) + \sum_{s=1, s \neq r}^N e_s \Gamma_s \right] \quad (25)$$

Note that the only source of internal energy being considered here is that due to "flow work". This is required for the compressible flow formulation, but other terms, such as heat conduction are at times included.

- (9) *Compute Lagrangian phase quantities at cell-centers*: The increments in mass, momentum and energy computed above are added to their time t counterparts to get the Lagrangian values for these quantities. Note that here, some Lagrangian quantities are denoted by an L- superscript. This indicates that all physical processes have been accounted for except for inter-material exchange of momentum and heat which is described in the following step.

$$(m)_r^L = (m)_r^t + \Delta(m)_r \quad (26)$$

$$(m\mathbf{u})_r^{L-} = (m\mathbf{u})_r^t + \Delta(m\mathbf{u})_r \quad (27)$$

$$(me)_r^L = (me)_r^t + \Delta(me)_r \quad (28)$$

- (10) *Momentum and heat exchange*: The exchange of momentum and heat between materials is computed according to:

$$(m\mathbf{u})_r^L = (m\mathbf{u})_r^{L-} + \Delta t m_r \sum_{s=1}^N \theta_r \theta_s K_{rs} (\mathbf{u}_s^L - \mathbf{u}_r^L) \quad (29)$$

$$(me)_r^L = (me)_r^{L-} + \Delta t m_r c_{v_r} \sum_{s=1}^N \theta_r \theta_s H_{rs} (T_s^L - T_r^L) \quad (30)$$

These equations are solved in a pointwise implicit manner that allows arbitrarily large momentum transfer to take place between materials. Typically, in FSI solutions, very large (10^{15}) values of K are used, which results in driving contacting materials to the same velocity. Inter-material heat exchange is usually modeled at a lower rate. Again, note that the same operation must be done following Step 3 above in the computation of the face-centered velocities.

- (11) *Specific volume evolution:* As discussed above in step 2, in order to correctly compute the equilibrium pressure and the volume fraction, it is necessary to keep an accurate accounting of the specific volume for each material. Here, we compute the evolution in specific volume due to the changes in temperature and pressure, as well as phase change, during the foregoing Lagrangian portion of the calculation, according to:

$$\Delta(mv)_r = \Delta t V \left[v_r \Gamma_r + f_r^\theta \nabla \cdot \sum_{s=1}^N \theta_s^* \mathbf{u}_s^* + \theta_r \beta_r \dot{T}_r - f_r^\theta \sum_{s=1}^N \theta_s \beta_s \dot{T}_s \right] \quad (31)$$

$$(mv)_r^L = (mv)_r^t + \Delta(mv)_r \quad (32)$$

where β is the constant pressure thermal expansivity and $\dot{T} = \frac{T^L - T^t}{\Delta t}$ is the rate of change of each material's temperature during the Lagrangian phase of the computation.

- (12) *Advect fluids:* For the fluid phase, use a suitable advection scheme, such as that described in [15], to transport mass, momentum, internal energy and specific volume. As this last item is an intensive quantity, it is converted to material volume for advection, and then reconstituted as specific volume for use in the subsequent timestep's equilibrium pressure calculation.
- (13) *Update nodal quantities for solid materials:* Those changes in solid material mass, momentum and internal energy that are computed at the cell-centers are interpolated to the nodes as field quantities, e.g., changes in momentum are expressed as accelerations, for use in Eq. (15).
- (14) *Advect solids:* For the solid phase, interpolate the time advanced grid velocity and the corresponding velocity increment (acceleration) back to the particles, and use these to advance the particle's position and velocity, according to Eqs. (16) and (17).

This completes one timestep. In the preceding, the user has a number of options in the implementation. The approach taken here was to develop a working MPM code and a separate working multi-material ICE code. In addition, some routines specific to the integration are required, for example, to transfer data from grid nodes to cell-centers. We note, however, that the fluid structure interaction methodology should not be looked at in the context of a “marriage” between an Eulerian CFD code and MPM.

The underlying theory is a multi-material description that has the flexibility to incorporate different numerical descriptions for solid and fluid fields within the overarching solution process. To have flexibility in treating a widest range of problems, it was our desire that in the integration of the two algorithms, each of the components be able to function independently. As described here, this method is fully explicit in time. To make this implicit with respect to the propagation of pressure waves, a Poisson equation is solved in the calculation of Δp , which is in turn used to iteratively update the face-centered velocities [8].

4. Models

The governing equations given in Section 2 are incomplete without closure equations for quantities such as pressure, stress, and rate of exchange of mass between materials. Equations of state, constitutive models and reaction models provide the needed closure. Brief descriptions of some of the models used in this work are given below.

4.1. High energy material reaction models

Two types of High Energy (HE) reaction models were considered here. The first is a model for detonation, in which the reaction front proceeds as a shock wave through the solid reactant, leaving highly pressurized product gases behind the shock. The second is a deflagration model, in which the reaction proceeds more slowly through the reactant in the form of a thermal burn. Each is described here.

4.1.1. The JWL++ detonation model

The detonation model used in two of the calculations discussed in Section 5 is a reactive flow model known as JWL++ [16]. JWL++ consists of equations of state for the reactant and the products of reaction as well as a rate equation governing the transformation from product to reactant. In addition, the model consists of a “mixer” which is a rule for determining the pressure in a mixture of product and reactant, as found in a partially reacted cell. Because pressure equilibration among materials is already part of the multi-material CFD formulation described in Section 3, the mixer was not part of the current implementation. Lastly, two additional rules apply. The first is that reaction begins in a cell when the pressure in that cell exceeds 200 MPa. Finally, no more than 20% of the explosive in a cell is allowed to react in a given timestep.

The Murnaghan equation of state [17] used for the solid reactant material is given by:

$$p = \frac{1}{nk} \left(\frac{1}{v^n} - 1 \right) \quad (33)$$

where $v = \rho_0/\rho$, and n and k are material dependent model parameters. Note that while the reactants are solid materials, they are assumed to not support deviatoric stress. Since a detonation propagates faster than shear waves, the strength in shear of the reactants can be neglected. Since

it is not necessary to track the deformation history of a particular material element, in this case, the reactant material was tracked only in the Eulerian frame, *i.e.* not represented by particles within MPM.

The JWL C-term form is the equation of state used for products, and is given by:

$$p = A \exp(-R_1 v) + B \exp(-R_2 v) + \frac{C}{\rho_0 \kappa v^{n-1}} \quad (34)$$

where A , B , C , R_1 , R_2 , ρ_0 and κ are all material dependent model parameters.

The rate equation governing the transformation of reactant to product is given by:

$$\frac{dF}{dt} = G(p + q)^b (1 - F) \quad (35)$$

where G is a rate constant, and b indicates the power dependence on pressure. q is an artificial viscosity, but was not included in the current implementation of the model. Lastly:

$$F = \frac{\rho_{\text{product}}}{\rho_{\text{reactant}} + \rho_{\text{product}}} \quad (36)$$

is the burn fraction in a cell. This can be differentiated and solved for a mass burn rate in terms of dF :

$$\Gamma = \frac{dF}{dt} (\rho_{\text{reactant}} + \rho_{\text{product}}) \quad (37)$$

This detonation model is empirically based and was designed to be simple and efficient, and while it works well for the geometries employed here, it may not be suitable for all applications. Implementation of other models within the algorithmic and computational framework described here is straightforward.

4.1.2. Deflagration model

The rate of thermal burning, or deflagration, of a monopropellant solid explosive is typically assumed to behave as:

$$D = Ap^n \quad (38)$$

where D can be thought of as the velocity at which the burn front propagates through the reactant (with units of length/time) and p is the local pressure [18]. A and n are parameters that are empirically determined for particular explosives. Because deflagration is a surface phenomena, our implementation requires the identification of the surface of the explosive. The surface is assumed to lie within those cells which have the highest gradient of mass density of the reactant material. Within each surface cell, an estimate of the surface area a is made based on the direction of the gradient, and the rate D above is converted to a mass burn rate by:

$$\Gamma = aD\rho_{\text{reactant}} \quad (39)$$

where ρ_{reactant} is the local density of the explosive. While the reaction rate is independent of temperature, initiation of

the burn depends on reaching a threshold temperature at the surface.

Since the rate at which a deflagration propagates is much slower than the shear wave speed in the reactant, it is important to track its deformation as pressure builds up within the container. This deformation may lead to the formation of more surface area upon which the reaction can take place, and the change to the shape of the explosive can affect the eventual violence of the explosion. Because of this, for deflagration cases, the explosive is represented by particles in the Lagrangian frame. The stress response is treated by an implementation of ViscoSCRAM [19], which includes representation of the material's viscoelastic response, and considers effects of micro-crack growth within the granular composite material.

4.2. Constitutive model for container break-up

One of the unique features of the approach described here is its ability to treat the interaction of fluid regions that are initially separated by a solid material. Such a situation is found when gaseous products of reaction are contained in a metal canister surrounded by air. When the pressure within the container is sufficient, it will rupture and the product material will be in direct contact with the surrounding air. Given the ability to treat these situations, it is worthwhile to accurately describe the failure of the container.

While a full exposition of metal plasticity and failure is beyond the scope of this manuscript, a brief description of the current implementation is given here. More details of the models and algorithms, as well as validation of these models against experimental data, can be found elsewhere [20–22].

The Cauchy stress in the metal container was additively decomposed into a volumetric component and a deviatoric component. The deviatoric part of the stress is modeled using hypoelasticity, while the pressure behaves according to an equation of state. The Green–Naghdi stress rate [23,32] is used to provide objectivity to the constitutive equation. The assumption of an additive decomposition of the rate of deformation into elastic and plastic parts was made for this work, even though a multiplicative decomposition as described by other investigators [25–29] is likely more appropriate, and will be considered in future works.

The volumetric stress is computed using a Mie–Grüneisen equation of state [30]:

$$p = \frac{\rho_0 C_0^2 (\eta - 1) [\eta - \frac{\Gamma_0}{2}(\eta - 1)]}{[\eta - S_x(\eta - 1)]^2} + \Gamma_0 E; \quad \eta = \rho/\rho_0 \quad (40)$$

where p is the pressure, C_0 is the bulk speed of sound, Γ_0 is the Grüneisen's gamma at the reference state, S_x is a linear Hugoniot slope coefficient, E is the internal energy per unit reference volume, ρ_0 is the initial density, and ρ is the current density,

In the elastic domain, the deviatoric stress is computed using a hypoelastic model with a constant shear modulus. The von Mises yield condition is used to determine whether the material is in the plastic domain. The flow stress (σ_y) is computed using the Johnson–Cook model [31]:

$$\sigma_y(\epsilon_p, \dot{\epsilon}_p, T) = \sigma_0 \left[1 + \frac{B}{\sigma_0} (\epsilon_p)^n \right] \left[1 + C \ln(\dot{\epsilon}_p^*) \right] \left[1 - (T^*)^m \right] \quad (41)$$

$$\dot{\epsilon}_p^* = \frac{\dot{\epsilon}_p}{\dot{\epsilon}_{p0}}; \quad T^* = \frac{(T - T_0)}{(T_m - T_0)} \quad (42)$$

where σ_0 is the yield stress at zero plastic strain, and (B, C, n, m) are material constants, ϵ_p is the equivalent plastic strain, $\dot{\epsilon}_p$ is the plastic strain rate, $\dot{\epsilon}_{p0}$ is a reference strain rate, T_0 is a reference temperature, and T_m is the melt temperature.

The plastic strain and the deviatoric Cauchy stress in the plastic domain are computed with a semi-implicit stress update algorithm [24,23]. A portion of the plastic work is converted into heat using a Taylor–Quinney coefficient of 0.9. The temperature of a material point is updated accordingly.

Experiments show that metal containers fail both by void nucleation and growth and by adiabatic shear banding. We use three criteria to determine whether a material point has failed.

- (1) *Melting*: A material point is tagged as “failed” when its temperature is greater than the melting point of the material at the applied pressure.
- (2) *TEPLA-F failure condition*: A material point is also assumed to have failed when the TEPLA-F failure criterion [33] is satisfied. This criterion can be written as

$$(f/f_c)^2 + (\epsilon_p/\epsilon_p^f)^2 = 1 \quad (43)$$

where f is the current porosity, f_c is the maximum allowable porosity, ϵ_p is the current plastic strain, and ϵ_p^f is the plastic strain at fracture. The evolution of porosity is given by [34,35]:

$$\dot{f} = \dot{f}_{\text{nuc}} + \dot{f}_{\text{grow}} \quad (44)$$

$$\dot{f}_{\text{grow}} = (1 - f) \text{tr}(\mathbf{D}_p) \quad (45)$$

$$\dot{f}_{\text{nuc}} = \frac{f_n}{(s_n \sqrt{2\pi})} \exp \left[-\frac{1}{2} \frac{(\epsilon_p - \epsilon_n)^2}{s_n^2} \right] \dot{\epsilon}_p \quad (46)$$

where \mathbf{D}_p is the rate of plastic deformation tensor, f_n is the volume fraction of void nucleating particles, ϵ_n is the mean of the distribution of nucleation strains, and s_n is the standard deviation of the distribution. A gaussian distribution of initial porosity is assumed.

The plastic strain at fracture is determined using the Johnson–Cook damage model [36]:

$$\begin{aligned} \epsilon_p^f &= \left[D_1 + D_2 \exp \left(\frac{D_3}{3} \sigma^* \right) \right] \left[1 + D_4 \ln(\dot{\epsilon}_p^*) \right] \left[1 + D_5 T^* \right]; \\ \sigma^* &= \frac{\text{tr}(\boldsymbol{\sigma})}{\sigma_{\text{eq}}} \end{aligned} \quad (47)$$

where D_1, D_2, D_3, D_4, D_5 are material constants, $\boldsymbol{\sigma}$ is the Cauchy stress, and T^* is the homologous temperature. We assume that the plastic strains at failure are also distributed in a gaussian manner. The distribution of fracture strains is simulated by evolving an internal damage variable based on the plastic strain and by initializing the damage variable to a non-zero value at the beginning of the simulation.

- (3) *Loss of material stability*: The third criterion that is used to determine failure is the loss of material stability of the solid. Since this condition is not sufficient to determine failure, we check two conditions – the Drucker stability condition [37] and the loss of hyperbolicity of the governing equations (the determinant of the acoustic tensor changes sign) [38,39].

Determination of the acoustic tensor requires a search for a normal vector around the material point and is therefore computationally expensive. A simplification of this criterion is a check which assumes that the direction of instability lies in the plane of the maximum and minimum principal stress [40]. In this approach, we assume that the strain is localized in a band with normal \mathbf{n} , and the magnitude of the velocity difference across the band is \mathbf{g} . Then the bifurcation condition leads to the relation

$$R_{ij}g_j = 0; \quad R_{ij} = M_{ijkl}n_k n_l + M_{ilkj}n_k n_l - \sigma_{ik}n_j n_k \quad (48)$$

where M_{ijkl} are the components of the co-rotational tangent modulus tensor and σ_{ij} are the components of the co-rotational stress tensor. If $\det(R_{ij}) \leq 0$, then g_j can be arbitrary and there is a possibility of strain localization.

If this condition for the loss of hyperbolicity is met, a material point deforms in an unstable manner and failure is assumed to have occurred at that point.

After it has been determined that a material point has failed, the stress at that point is set to zero – indicating that a free surface has been created. As the simulation evolves, cracks develop in the material around the failed particles ultimately leading to the break-up of the container.

5. Numerical results

The simulation results presented here are intended to serve two purposes, to validate the method presented above, and to demonstrate its capabilities. While results from some very basic validation tests, as well as an order or accuracy study, can be found in [41,42], those presented here are targeted toward exploding energetic devices. Additional validation tests of an intermediate degree of complexity would be an ideal addition to what is presented

here, but the availability of theoretical solutions or experimental data for such cases is not good. In contrast, extensive experimental data have been collected for the first two cases shown here, and these data are compared with simulation results. The first test, detonation of a series of cylinders of explosive, validates both the general multi-material framework, including material transformation, as well as the detonation model itself. In the second test, a cylinder of explosive confined in a copper tube is detonated. There, the confidence gained from the first test is built upon and extended to include the interaction of the highly pressurized product gases with the confining copper cylinder. Wall velocity of the copper tube is compared with experimental measurements.

For the last case, a steel cylinder filled with PBX-9501 is heated to the critical temperature to commence a deflagration. The simulation continues through the rupture of the case when product gases are free to interact with the surrounding air. This simulation demonstrates a unique capability of this approach, in which initially separate fluid regions are allowed to interact following the failure of the steel container. While previous calculations give some confidence in the validity of this calculation, it does make use of models which have not been fully validated, and as such, should be considered a prediction.

5.1. Rate stick simulations

A well known phenomenon of detonating solid high explosives is the so-called “size effect”. The size effect refers to the change of the steady state detonation velocity of explosives, U_s with size R_0 [16]. In order to validate our implementation of the JWL++ detonation model within our multi-material framework, a parameter study was conducted for cylinders of Ammonium Nitrate Fuel Oil (ANFO-K1) with length of 10 cm and radii ranging from 4 mm to 20 mm. In addition, a one-dimensional simulation provided for the “infinite radius” case. In each of the finite radius cases, the cylinder was initially surrounded by air. Detonation was initiated by impacting the cylinder at 90 m/s against the boundary of the computational domain, at which a zero velocity Dirichlet boundary condition was imposed. This impact was sufficient to raise the pressure within the cylinder to above the threshold for initiation of reaction. The detonation velocity was determined by comparing the arrival time of the detonation at two points along the cylinder, sufficiently into the far field that the detonation had reached a steady state.

Material properties for these cases included the following. The reactant was described by a Murnaghan equation of state with parameters $n = 7.4$, $\kappa = 3.9 \times 10^{11} \text{ Pa}^{-1}$ and $\rho_0 = 1160.0 \text{ kg/m}^3$. The products of reaction were described by a JWL C-term form equation of state with parameters $A = 2.9867 \times 10^{11} \text{ Pa}$, $B = 4.11706 \times 10^9 \text{ Pa}$, $C = 7.206147 \times 10^8 \text{ Pa}$, $R_1 = 4.95$, $R_2 = 1.15$, $\omega = .35$ and $\rho_0 = 1160.0 \text{ kg/m}^3$. The JWL++ parameters were taken as: $G = 3.5083 \times 10^{-7} \text{ s}^{-1} \text{ Pa}^b$, $b = 1.3$, $\rho_0 = 1160.0 \text{ kg/m}^3$. In

all, this simulation included three materials; the reactant material, the products of reaction and the surrounding air.

Simulations were carried out on uniform meshes with cell sizes of 1.0 mm, 0.5 mm and 0.25 mm. A one-quarter symmetry was assumed in all cases. A qualitative representation is shown in Fig. 2, which depicts a volume rendering of the density of the reactant as the detonation has progressed about halfway into the material for the 12 mm radius case at the finest resolution. The curvature of the burn front and the elevated density just ahead of it are evident in this view.

Fig. 3 is a plot of detonation velocity vs. the inverse of the sample radius. Experimental data are represented by open squares, while results of the simulations are shown with filled circles ($h = 1.0 \text{ mm}$), filled diamonds ($h = 0.5 \text{ mm}$) and filled triangles ($h = 0.25 \text{ mm}$). Connecting lines for the numerical data are in place to guide the eyes of the reader. Evident from this plot is the convergence of detonation velocities with grid resolution, and the generally good agreement between experimental and computed detonation velocities at the finer grid resolutions, particularly at the larger radii, where both the experimental data and the model are considered more reliable. Better agreement with data could likely have been achieved by “tuning” the JWL++ parameters, a step which is commonly done to calibrate the model with a particular hydrodynamics code. That step was neglected here, as the radius at which the subsequent test was carried out is within the range at which good agreement exists for all resolutions. Note that “goodness” of fit has been judged solely by inspection, not by any analytical means.

Again, while this set of tests doesn’t validate the full fluid–structure interaction approach, it does give credibility to the underlying multi-material formulation, including the

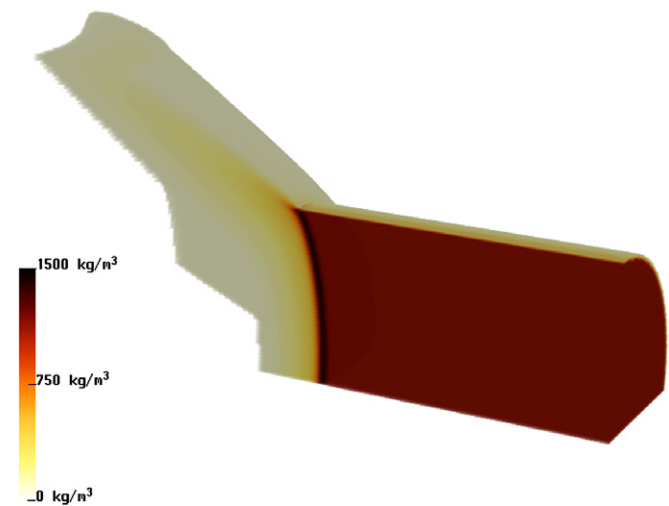


Fig. 2. Unconfined 12 mm “rate-stick”. The mass density of the reactant material is volume rendered, and shows evidence of the curvature of the reaction front, and the compression of the reactant just ahead of the reaction. Behind the detonation, most of the reactant material is consumed.

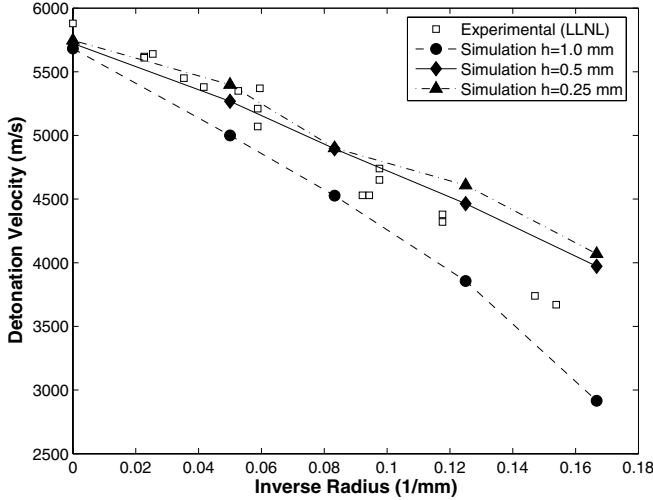


Fig. 3. Detonation velocity vs. inverse radius. Experimental and numerical data are presented, and indicate good agreement of the model with experiment, as well as convergence of detonation velocity with grid resolution.

pressure equilibration and the exchange of mass between materials, in this case as governed by the JWL++ detonation model, as well as momentum and energy.

5.2. Cylinder test simulation

The cylinder test is an experiment which is frequently used to calibrate equations of state for detonation products of reaction [43]. In this case, the test consists of an oxygen free, high conductivity (OFHC) copper tube with an inner radius of 2.54 cm, an outer radius of 3.06 cm and a length of 35 cm. The tube is filled with QM-100, an Ammonium Nitrate emulsion, and a detonation is initiated at one end of the tube. Measurements of the wall velocity wall are made at individual points along the length of the tube using Fabry–Perot interferometry or streak cameras.

A simulation of this configuration was performed and wall velocity data were collected at an axial location 25 cm from the point of initiation. The reactant was again described by a Murnahan equation of state with parameters $n = 7.0$, $\kappa = 1.02 \times 10^{-9} \text{ Pa}^{-1}$ and $\rho_0 = 1260.0 \text{ kg/m}^3$. The products of reaction were described by a JWL C-term form equation of state with parameters $A = 4.8702 \times 10^{11} \text{ Pa}$, $B = 2.54887 \times 10^9 \text{ Pa}$, $C = 5.06568 \times 10^8 \text{ Pa}$, $R_1 = 5.0$, $R_2 = 1.0$, $\omega = .3$ and $\rho_0 = 1260.0 \text{ kg/m}^3$. The JWL++ parameters were taken as: $G = 9.1 \times 10^{-5} \text{ s}^{-1}$ Pa , $b = 1.0$, $\rho_0 = 1260.0 \text{ kg/m}^3$. The copper tube was modeled as an elastic–plastic material with a density of 8930.0 kg/m^3 , bulk and shear moduli of 117.0 GPa and 43.8 GPa , respectively, and a yield stress of 70.0 MPa . The copper tube was surrounded by air. In all, 4 materials are present in this simulation, the reactant, the products of reaction, the copper tube, and the surrounding air.

Again, a one-quarter symmetry section of the full cylinder was modeled using a cell size of $h = 0.5 \text{ mm}$ and a total domain size of $35 \text{ cm} \times 6 \text{ cm} \times 6 \text{ cm}$. Zero gradient conditions described the exterior boundaries, which allowed material to exit the domain.

Fig. 4 shows a snapshot of this test midway through the simulation, at $t = 18.8 \mu\text{s}$. The copper tube is depicted using an iso-surface of the cell-centered mass density (the two surfaces are the inner and outer walls of the tube) that is colored by velocity. A volume rendering of the pressure field is also present. Alternating bands of high and low velocity of the tube wall are evidently due to the reflection

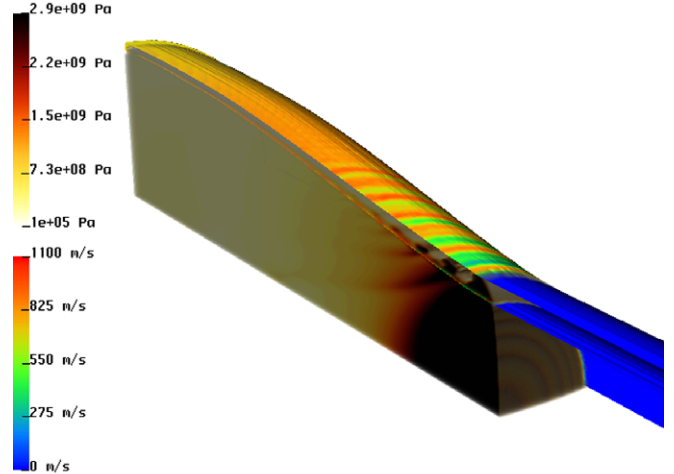


Fig. 4. Copper cylinder test simulation. The walls of the copper tube are depicted as an isosurface of density of the copper material and are colored by velocity magnitude. Pressure is represented by a volume rendering, and indicates the progress of the detonation, as well as the interaction of the pressurized products of reaction with the confining walls.

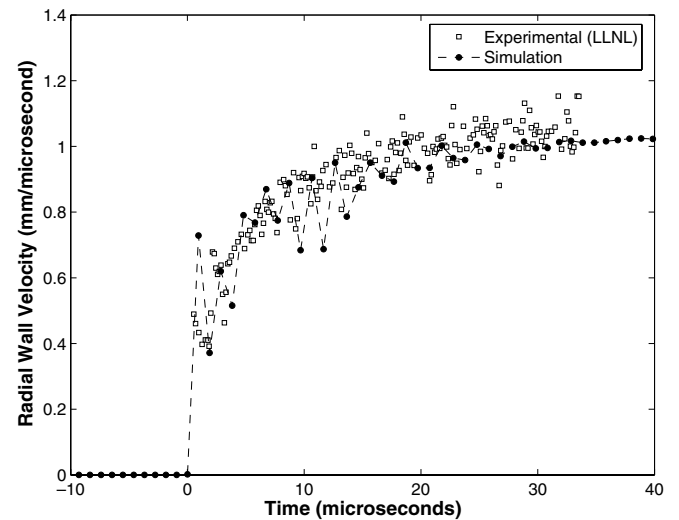


Fig. 5. Copper cylinder test simulation. Experimental and computational velocities of the cylinder vs. time. Data was collected at a point 25 cm from the point of initiation of the detonation.

Table 1
Material constants for 4340 steel

ρ (kg/m ³)	K (GPa)	μ (GPa)	T_0 (K)	T_m (K)	C_0 (m/s)	Γ_0	S_x		
7830.0	173.3	80.0	294.0	1793.0	3574	1.69	1.92		
A (MPa)	B (MPa)	C	n	m	D_1	D_2	D_3	D_4	D_5
792.0	510.0	0.014	0.26	1.03	0.05	3.44	-2.12	0.002	0.61

of the impulse provided by the shock between the inner and outer surfaces of the tube.

Velocity data was collected from those particles which were both initially at an axial location of 25 cm, and upon the exterior surface of the tube. The velocity from this collection of particles was averaged over the circumference and plotted vs. time in Fig. 5. In addition, experimental results (LLNL, Shot No. K260-581) are also shown. Both datasets are time shifted to coincide with the arrival of the detonation. Visual inspection of the data indicates reasonably good agreement between the experimental and numerical data. There are some differences in the high frequency component of the datasets, but without multiple sets of experimental data against which to compare, it is difficult to know how much of this deviation is due to experimental uncertainty. Further analysis of both the numerical and experimental data would be required to deem this case fully validated, but these results provide confidence in the ability of this approach to generate meaningful results for scenarios such as this.

5.3. Fast cookoff simulation

Cookoff tests, generally speaking, refer to experiments in which energetic material is heated until it reaches ignition. The rate of heating typically differentiates these tests in to “fast” or “slow” cookoff. In slow cookoff tests, the temperature is usually increased very slowly, perhaps a few degrees per hour, so that the entire sample is able to equilibrate and is nearly isothermal when ignition occurs. In fast cookoff tests, heat is added to the system quickly, which is likely to lead to relatively local ignition at the surface of the sample. Fast cookoff is more likely to occur in an accident scenario, where ordinance may be subject to heating by a fire, as occurred on the USS Forrestal in 1967.

The scenario considered here consists of a cylindrical 4340 steel container with both inner diameter and length of 10.16 cm, and wall thickness of 0.635 cm, filled with PBX-9501. The temperature of the container was initialized to be 1°K above the ignition temperature in the deflagration model for PBX-9501. In this way, the entire outer surface of the explosive is ignited simultaneously. This is, of course, somewhat unrealistic for an accident scenario, but rather is an idealization. Additionally, while the deflagration model described in Section 4.1.2 is used throughout the simulation, it is possible for deflagrations, also known as thermal burns, to transition to detonation (DDT). However, the physics governing DDT are not yet well under-

stood, and good numerical models to describe the phenomenon are not yet available.

Mechanical properties for PBX 9501 were obtained from the literature [19], while the material constants used in the modeling of 4340 steel are shown in Table 1. A temperature-dependent specific heat model [44] was used to compute the internal energy and the rate of temperature increase in the material. We assumed an initial mean porosity of 0.005 with a standard deviation of 0.001. The critical porosity was 0.3. The mean strain at void nucleation was assumed to be 0.3 with a standard deviation of 0.1. The scalar damage variable was initialized with a mean of 0.005 and a standard deviation of 0.001.

Three planes of symmetry are assumed, which allows modeling only 1/8th of the total geometry. Each dimension of the computational domain was 9.0 cm discretized into 180 computational cells, for a grid spacing of $h = 0.5$ mm. Four materials were present, the steel container and the PBX-9501, each of which are treated in the Lagrangian frame of reference, as well as the air initially surrounding the container, and the products of reaction from the deflagration, both of which are represented in the Eulerian frame of reference. Neumann zero gradient boundary conditions were used on the exterior domain boundaries to allow material to flow out of the domain, as the explosion progressed.

Results from this simulation are shown in Fig. 6. In each panel, the container and explosive are depicted by isosurfaces, blue and red, respectively. In Fig. 6b–e, a volume rendering of the mass density of the product material of the reaction is also included. Fig. 6a shows the initial state of the geometry, while the remaining panels show the progression of the simulation at the times indicated in the captions. The last two panels depict the same time, with the product gas removed in the final panel, to more clearly show the state of the container at that time. Close comparison of the initial and final panels also reveals the reduction in size of the explosive pellet, due to the reaction. Product gas first begins to leave the container through a rupture where the side and end of the container meet (Fig. 6c), and ultimately also through a rupture in middle (Fig. 6e). The formation of these openings is governed by material localization as described in Section 4.2.

Since no surface tracking is required in this method, there is no requirement to track the creation of the new surfaces that occur due to material failure. Gas is free to escape through the openings simply because there is no longer anything in those computational cells to prevent it once the gap is sufficiently wide.

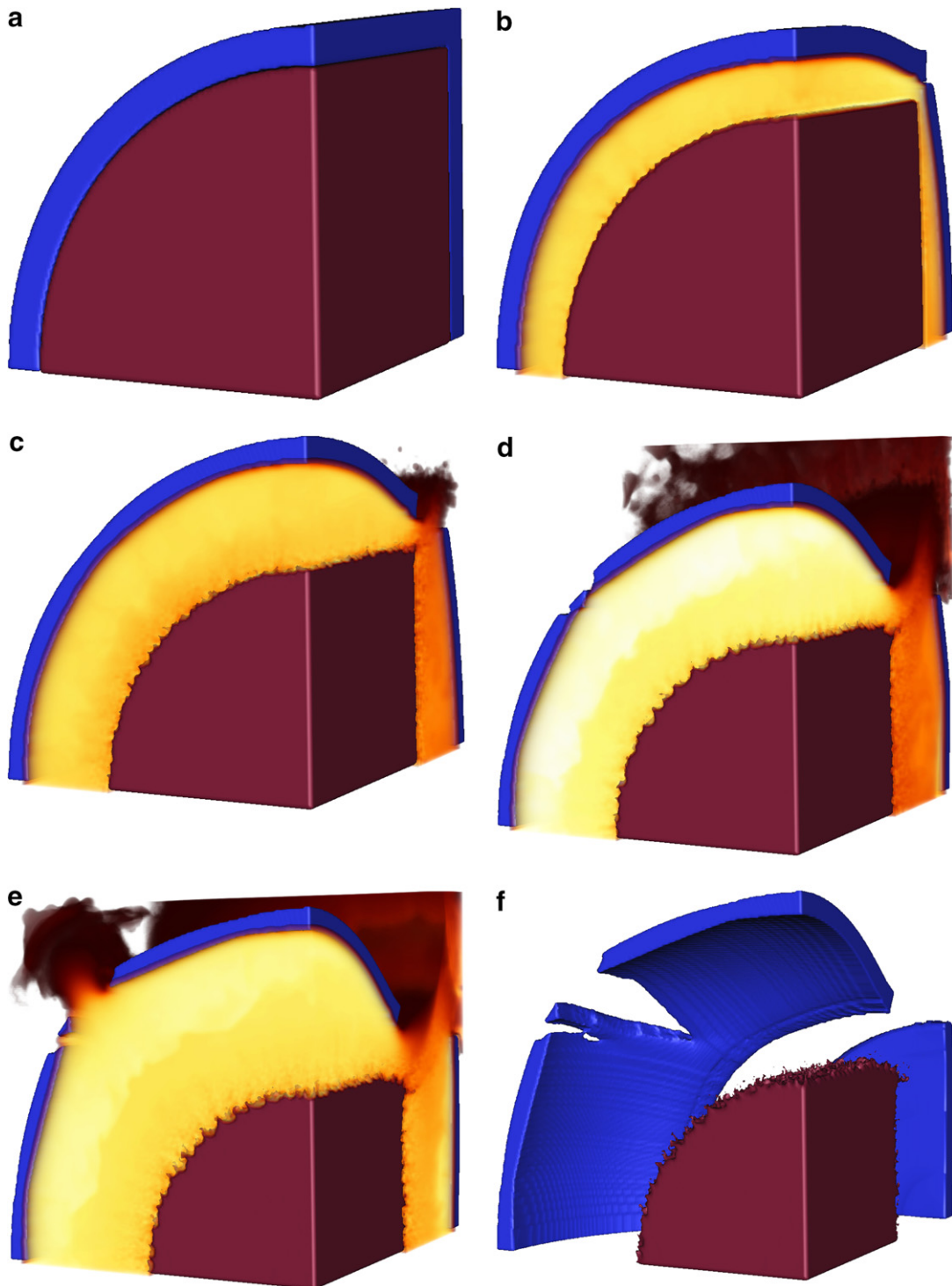


Fig. 6. Time series of a steel container (blue) filled with deflagrating plastic bonded explosive (red). A volume rendering of the mass density of the products of reaction is also shown, except in the final 0 panel, where it is removed to more clearly show the regions where the container has failed. (a) $t = 0$ ms, (b) $t = .137$ ms, (c) $t = .203$ ms, (d) $t = .259$ ms, (e) $t = .312$ ms, (f) $t = .312$ ms. (For interpretation of the references in color in this figure legend, the reader is referred to the web version of this article.)

6. Conclusions

An approach for solving full-physics fluid–structure interaction scenarios has been presented which uses an Eulerian frame description for fluids and a Lagrangian

frame description for solids. The equations governing the behavior of these materials, including their interactions, are based on an averaged model approach, which eliminates the need to maintain a description of the interface between the materials. In addition to allowing for arbitrary

distortion of material interfaces, the treatment of solid to gas phase reactions is also facilitated by this approach.

The validation calculations presented here give a high degree of confidence in the quality of the solutions obtained by this method, while the final demonstration calculation indicates the complexity of the situations that can be considered. It is important to point out, however, that in the authors' experience, this approach is best suited to high deformation rate problems, and may do less well in situations where the solid is loaded more slowly. This is true for two reasons. First, while making the algorithm implicit in time with respect to pressure is relatively straightforward, doing so with respect to the stress waves in the solid is less so. Implicit versions of MPM have been implemented with success, but the strategy for incorporating any of these within the integrated formulation is not obvious, and may require making the entire algorithm fully implicit in time. Second, as a method for solid mechanics, currently MPM is best suited for highly dynamic loading, although improvements are continuously being made that should improve its performance in quasi-static scenarios.

In order to improve the efficiency of calculations, a structured adaptive mesh refinement (SAMR) strategy is being pursued that will allow resources to be concentrated on those parts of the domain where they are needed. The current implementation allows for the solid materials described using MPM to be advanced at a single level of resolution, while those materials integrated in the Eulerian frame are advanced on an arbitrary number of levels of resolution. Thus, in the final simulation shown here, the container and solid explosive, which require the greatest degree of resolution to accurately compute the phase transformation and material response, can be represented on the finest level. Meanwhile the region away from the device can advance at a lower spatial resolution until container expansion and rupture dictate the need for refinement. This strategy enhances the range of simulations that can be considered, reduces the required computational time and lowers the requirement for the storage of data.

Acknowledgements

The authors gratefully acknowledge Dr. Bryan A. Kashiwa of Los Alamos National Laboratory for sharing with us the theoretical and algorithmic foundations upon which this work is based. Without the personal interactions that he made time to provide, none of this would be possible. The authors also wish to thank Dr. Clark Souers of Lawrence Livermore National Laboratory for providing the experimental rate stick and cylinder test data. This work was supported by the National Science Foundation's Information Technology Research Program under grant CTS0218574, and the US Department of Energy through the Center for the Simulation of Accidental Fires and Explosions, under grant W-7405-ENG-48.

References

- [1] Benson DJ. A multi-material Eulerian formulation for the efficient solution of impact and penetration problems. *Comput Mech* 1995;15: 557–8.
- [2] Benson DJ. Eulerian finite element methods for the micromechanics of heterogeneous materials: dynamic prioritization of material interfaces. *Comput Methods Appl Mech Engrg* 1998;151:343–60.
- [3] Sulsky D, Chen Z, Schreyer HL. A particle method for history dependent materials. *Comput Methods Appl Mech Engrg* 1994;118: 179–96.
- [4] Sulsky D, Zhou S, Schreyer HL. Application of a particle-in-cell method to solid mechanics. *Comput Phys Commun* 1995;87:236–52.
- [5] Kashiwa BA. A multifield model and method for fluid–structure interaction dynamics. Technical Report LA-UR-01-1136, Los Alamos National Laboratory, Los Alamos, 2001.
- [6] Kashiwa BA, Rauenzahn RM. A multimaterial formalism. Technical Report LA-UR-94-771, Los Alamos National Laboratory, Los Alamos, 1994.
- [7] Harlow FH, Amsden AA. Numerical calculation of almost incompressible flow. *J Comput Phys* 1968;3:80–93.
- [8] Kashiwa BA, Rauenzahn RM. A cell-centered ICE method for multiphase flow simulations. Technical Report LA-UR-93-3922, Los Alamos National Laboratory, Los Alamos, 1994.
- [9] Guilkey JE, Hoying JB, Weiss JA. Computational modeling of multicellular constructs with the material point method. *J Biomech* 2006;39:2074–86.
- [10] Brydon AD, Bardenhagen SG, Miller EA, Seidler GT. Simulation of the densification of real open-celled foam microstructures. *J Mech Phys Solids* 2005;53:2638–60.
- [11] Guo Y, Nairn JA. Calculation of *J*-integral and stress intensity factors using the material point method. *Comput Model Engrg Sci* 2004;6:295–308.
- [12] Brackbill JU, Ruppel HM. Flip: a low-dissipation, particle-in-cell method for fluid flows in two dimensions. *J Comput Phys* 1986; 65(24):314–43.
- [13] Bardenhagen SG, Kober EM. The generalized interpolation material point method. *Comput Model Engrg Sci* 2004;5:477–95.
- [14] Harlow FH, Amsden AA. Flow of interpenetrating material phases. *J Comput Phys* 1975;18:440–64.
- [15] VanderHeyden WB, Kashiwa BA. Compatible fluxes for van leer advection. *J Comput Phys* 1998;146:1–28.
- [16] Souers PC, Anderson S, Mercer J, McGuire E, Vitello P. JWL++: a simple reactive flow code package for detonation. *Propell Explos Pyrotechn* 2000;25:54–8.
- [17] Murnaghan FD. The compressibility of media under extreme pressures. *Proc Natl Acad Sci* 1944;30:244–7.
- [18] Son SF, Berghout HL, Bolme CA, Chavez DE, Naud D, Hiskey MA. Burn rate measurements of hmx, tattb, dht, daaf and btatz. *Proc Combust Inst* 2000;28:919–24.
- [19] Hackett RM, Bennett JG. Implicit finite element material model for energetic particulate composite materials. *Int J Numer Methods Engrg* 2000;49:1191–209.
- [20] Banerjee B. Simulation of impact and fragmentation with the material point method. In: Proc 11th international conference on fracture, Turin, Italy, 2005.
- [21] Banerjee B. The Mechanical Threshold Stress model for various tempers of AISI 4340 steel. *Int J Solids Struct* 2007;44(3–4):834–59.
- [22] Banerjee B. An evaluation of plastic flow stress models for the simulation of high-temperature and high strain-rate deformation of metals. arXiv:cond-mat 2005;0512466:1–43.
- [23] Maudlin PJ, Schiferl SK. Computational anisotropic plasticity for high-rate forming applications. *Comput Methods Appl Mech Engrg* 1996;131:1–30.
- [24] Nemat-Nasser S. Plasticity: a treatise on finite deformation of heterogeneous inelastic materials. Cambridge: Cambridge University Press; 2004.

- [25] Kojic M, Bathe KJ. Inelastic analysis of solids and structures. New York: Springer; 2005.
- [26] Eterovic AL, Bathe KJ. A hyperelastic-based large strain elastoplastic constitutive formulation with combined isotropic-kinematic hardening using logarithmic stress and strain measures. *Int J Numer Methods Engrg* 1990;30:1099–114.
- [27] Scheidler M, Wright TW. A continuum framework for finite viscoplasticity. *Int J Plasticity* 2001;17:1033–85.
- [28] Weber G, Anand L. Finite deformation constitutive equations and a time integration procedure for isotropic, hyperelastic–viscoplastic solids. *Comput Methods Appl Mech Engrg* 1990;79(25):173–202.
- [29] Geers MGD. Finite strain logarithmic hyperelasto-plasticity with softening: a strongly non-local implicit gradient framework. *Comput Methods Appl Mech Engrg* 2004;193:3377–401.
- [30] Zocher MA, Maudlin PJ, Chen SR, Flower-Maudlin EC. An evaluation of several hardening models using Taylor cylinder impact data. In: Proc European congress on computational methods in applied sciences and engineering, Barcelona, Spain, 2000. ECCOMAS.
- [31] Johnson GR, Cook WH. A constitutive model and data for metals subjected to large strains, high strain rates and high temperatures. In: Proc 7th international symposium on ballistics, 1983. p. 541–7.
- [32] Nemat-Nasser S. Rate-independent finite-deformation elastoplasticity: a new explicit constitutive algorithm. *Mech Mater* 1991;11:235–49.
- [33] Johnson JN, Addessio FL. Tensile plasticity and ductile fracture. *J Appl Phys* 1988;64(12):6699–712.
- [34] Chu CC, Needleman A. Void nucleation effects in biaxially stretched sheets. *ASME J Engrg Mater Tech* 1980;102:249–56.
- [35] Ramaswamy S, Aravas N. Finite element implementation of gradient plasticity models. Part II: Gradient-dependent evolution equations. *Comput Methods Appl Mech Engrg* 1998;163:33–53.
- [36] Johnson GR, Cook WH. Fracture characteristics of three metals subjected to various strains, strain rates, temperatures and pressures. *Int J Engrg Fract Mech* 1985;21:31–48.
- [37] Drucker DC. A definition of stable inelastic material. *J Appl Mech* 1959;26:101–6.
- [38] Rudnicki JW, Rice JR. Conditions for the localization of deformation in pressure-sensitive dilatant materials. *J Mech Phys Solids* 1975;23:371–94.
- [39] Perzyna P. Constitutive modelling of dissipative solids for localization and fracture. In: Perzyna P, editor. Localization and fracture phenomena in inelastic solids. CISM courses and lectures, vol. 386. New York: SpringerWien; 1998. p. 99–241.
- [40] Becker R. Ring fragmentation predictions using the Gurson model with material stability conditions as failure criteria. *Int J Solids Struct* 2002;39:3555–80.
- [41] Guilkey JE, Harman TB, Xia A, Kashiwa BA, McMurtry PA. An Eulerian–Lagrangian approach for large deformation fluid–structure interaction problems, part 1: Algorithm development. In: Fluid structure interaction II. Cadiz, Spain: WIT Press; 2003.
- [42] Harman TB, Guilkey JE, Kashiwa BA, Schmidt J, McMurtry PA. An Eulerian–Lagrangian approach for large deformation fluid–structure interaction problems, part 1: Multi-physics simulations within a modern computational framework. Fluid structure interaction II, vol. 26. Cadiz, Spain: WIT Press; 2003.
- [43] Souers PC, Forbes JW, Fried LE, Howard WM, Anderson S, Dawson S, et al. Detonation energies from the cylinder test and cheetah v3.0. *Propell Explos Pyrotech* 2001;26:180–90.
- [44] Goto DM, Bingert JF, Chen SR, Gray GT, Garrett RK. The mechanical threshold stress constitutive-strength model description of HY-100 steel. *Metall Mater Trans A* 2000;31A(27):1985–96.